scientific reports

OPEN

Large bi-axial tensile strain effect in epitaxial BiFeO$_3$ film grown on single crystal PrScO$_3$

In-Tae Bae[1✉], Zachary R. Lingley[1], Brendan J. Foran[1], Paul M. Adams[2] & Hanjong Paik[3,4]

A BiFeO$_3$ film is grown epitaxially on a PrScO$_3$ single crystal substrate which imparts ~ 1.45% of biaxial tensile strain to BiFeO$_3$ resulting from lattice misfit. The biaxial tensile strain effect on BiFeO$_3$ is investigated in terms of crystal structure, Poisson ratio, and ferroelectric domain structure. Lattice resolution scanning transmission electron microscopy, precession electron diffraction, and X-ray diffraction results clearly show that in-plane interplanar distance of BiFeO$_3$ is the same as that of PrScO$_3$ with no sign of misfit dislocations, indicating that the biaxial tensile strain caused by lattice mismatch between BiFeO$_3$ and PrScO$_3$ are stored as elastic energy within BiFeO$_3$ film. Nano-beam electron diffraction patterns compared with structure factor calculation found that the BiFeO$_3$ maintains rhombohedral symmetry, i.e., space group of *R3c*. The pattern analysis also revealed two crystallographically distinguishable domains. Their relations with ferroelectric domain structures in terms of size and spontaneous polarization orientations within the domains are further understood using four-dimensional scanning transmission electron microscopy technique.

BiFeO$_3$ (BFO) is known as the only multiferroic material that exhibits ferroelectricity and *G*-type antiferromagnetism, simultaneously well above room temperature[1,2]. Thus, BFO has application potential for emerging spintronics technology such as multiple-state memory and magnetic random access memory[3–5]. Early studies on BFO suggested that ferroelectric response in BFO was weak, i.e., 3.5 μC cm^{-2}, in addition to the weak magnetic response, i.e., antiferromagnetism[1,6,7]. Thus, this material drew little attention. However, pioneering works in early 2000s demonstrated that its ferroelectric response is almost an order of magnitude higher than the previously reported value by showing that the spontaneous polarization value of BFO is ~ 60 μC cm^{-2}. This spontaneous polarization value has been reported for epitaxial BFO film[8] and high quality single crystalline bulk BFO[9,10]. In addition, with the availability of high quality single crystalline oxide substrates with lattice parameters and crystal structure that are similar to BFO, significantly increased spontaneous polarization values of 90–115 μC cm^{-2} were reported for epitaxially grown BFO films[11–14]. It is worth noting that the epitaxial BFO films are under biaxial strain caused by the difference in crystal symmetry and/or lattice parameter of the oxide substrate on which it grows. Furthermore, the biaxial strain caused by single crystal substrates with similar lattice parameter can be stored as *elastic* strain within BFO film rather than relaxed through lattice defect formations such as misfit dislocations. This is attributed to the structurally flexible nature of BFO that can accommodate many percent of elastic strain[15,16]. Since the elastic strain stored within BFO thin films modifies its lattice parameter and potentially crystal symmetry leading to changes in spontaneous polarization and magnetic property, considerable experimental and theoretical efforts have been devoted to understand the elastic strain effects on the crystal symmetry changes within epitaxial BFO films[11,17–20]. As a result, a variety of metastable BFO phases, such as rhombohedral[6] tetragonal-like[15,16,21–25], orthorhombic[26], orthorhombic-like monoclinic[27], monoclinic[24,28–32], and triclinic[33,34], are found depending on the substrate type and surface orientation of the substrate used. Interestingly, while extensive studies have already been performed to investigate the compressive strain effect on epitaxial BFO film, few studies have been performed for the tensile strain effect[32,35] presumably owing to the limited availability of high quality perovskite-based oxide substrates with the lattice parameters larger than that of BFO[36,37].

It is also worth noting that while most of the experimental works have used X-ray diffraction (XRD) techniques combined with pseudocubic notation-based BFO unit cell to investigate the misfit strain induced *unit cell distortion*, no discussion has been made on how the misfit strain affects *basis location* in the unit cell,

[1]Microeletronics Technology Department, The Aerospace Corporation, El Segundo, CA 90009, USA. [2]Materials Processing Department, The Aerospace Corporation, El Segundo, CA 90009, USA. [3]School of Electrical and Computer Engineering, University of Oklahoma, Norman, OK 73019, USA. [4]Center for Quantum Research and Technology, University of Oklahoma, Norman, OK 73019, USA. ✉email: intae.bae@aero.org

which is another important factor to properly evaluate a crystal structure. In order to address this issue, we have proposed to use hexagonal notation based BFO unit cell[27,38–42]. Since hexagonal notation describes rhombohedral unit cell of *unstrained* BFO impeccably, it has proven highly effective to accurately evaluate: (1) overall crystal symmetry and (2) the amount of misfit strain stored elastically within strain engineered BFO films. In addition, when structure factor calculations using hexagonal notation are compared with wide range reciprocal space information, such as nano-beam electron diffraction and/or X-ray reciprocal space mapping, it allows us to evaluate the crystal structure of elastically strained BFO with no ambiguity[27,35,38,39].

In this study, biaxial tensile strain in an epitaxial BFO film grown on a $PrScO_3$ (PSO) single crystal using molecular beam epitaxy is investigated as follows:

(1) Elastic strain induced BFO crystal structure is evaluated using aberration (C_s)-corrected scanning transmission electron microscopy (STEM) with nano-beam electron diffraction (NBED) and structure factor calculation.
(2) Quantitative strain measurement within the epitaxial BFO film is performed using precession electron diffraction (PED) in tandem with XRD and X-ray reciprocal space mapping.
(3) Ferroelectric domain structure and spontaneous polarization orientation within the domains are examined using four dimensional STEM differential phase contrast (4D STEM DPC) technique.

Results and discussion

Figure 1a shows a high angle annular dark field (HAADF)-STEM image of the BFO films grown on $(101)_o$ PSO substrate (space group: *Pnma*, $a = 0.5780$ nm, $b = 0.8025$ nm, $c = 0.5608$ nm, $\alpha = \beta = \gamma = 90°$) along $[\bar{1}11]_o$ zone axis (Subscript "o" denotes orthorhombic notation)[43]. It exhibits ~ 20 nm BFO grown on PSO substrate. Note that the BFO film shows up brighter than PSO substrate because Bi atom within BFO, which is heavier than Pr and Sc in PSO, provides more signals to the HAADF detector located at the collection semi-angle of 80–100 mrad[44].

To acquire information on the crystal structure of BFO and the epitaxial relation between BFO and PSO, nano-beam electron diffraction (NBED) patterns were recorded from BFO and PSO with a probe size of ~ 10 nm as shown in Fig. 1b,c. For accurate BFO phase identification in terms of: (1) lattice vector sizes and (2) basis locations in unit cell, structure factor, F_{hkl}, where hkl represents a specific Bragg's reflection, was calculated for all BFO phases discussed in previous reports (including theoretically predicted metastable ones) that provide all the necessary crystallographic information, such as space group, lattice parameter, and basis locations in unit cell[20,21,27,45,46]. These BFO phases are summarized in Table 1.

Also calculated was the structure factor of PSO substrate[43] to investigate the epitaxial relation with BFO overlayer. The electron diffraction calculation was based on kinematical approximation:

$$F_{hkl} = \sum_n f_n \exp\left[2\pi i\left(hx_n + ky_n + lz_n\right)\right],$$

where f_n is the atomic scattering factor for atom n at fractional coordinates (x_n, y_n, z_n). By comparing NBED patterns to the structure factor calculation results from all the BFO phases mentioned above, the NBED pattern from BFO layer shown in Fig. 1b is identified as the $[211]_h$ zone axis of rhombohedral BFO, i.e., bulk BFO crystal structure[45], as shown in the corresponding structure factor calculation of Fig. 1c. Note that (1) the $[211]_h$ orientation of rhombohedral BFO is based on three-index *hexagonal* notation (Subscript h denotes hexagonal notation) rather than pseudocubic (pc) notation that disregards: (1) ~ 0.55° of rhombohedral distortion and (2) basis locations in unit cell. However, since pc notation has been more widely used, we have summarized the relation between the hexagonal notations used in the current study and the corresponding pc notations in Table S1. The diffraction spots denoted by white arrows in Fig. 1b result from double diffraction, i.e., dynamical scattering effect, as discussed previously[27,35,38,39]. The Bragg's reflections denoted with yellow circles are indexed, for examples, $(11\bar{3})_h$, $(2\bar{1}\bar{3})_h$, $(\bar{1}13)_h$ and $(\bar{2}13)_h$ as shown in Fig. 1d (see Table S1 for the corresponding pc notations). Note that these are termed rhombohedral BFO signature reflections since none of the BFO phases (reported experimentally or theoretically) but rhombohedral BFO can produce them as discussed previously[27,38–40,42]. Since one of the critical structural characteristics of rhombohedral BFO is oxygen octahedral rotation, it is worth investigating whether oxygen octahedral rotation is preserved in this epitaxial BFO. Figure S1 show atomic models of (a) pseudocubic-approximated, i.e., perovskite (space group: $Pm\bar{3}m$; lattice parameter $a = 0.396$ nm) and (b) rhombohedral (space group: $R3c$), BFOs viewed along equivalent orientation, i.e., $[110]_{pc}$ for Fig. S1a, and $[110]_{pc}$, i.e., $[211]_h$, for Fig. S1), respectively. While no oxygen octahedral rotation shows in Fig. S1a, it is clearly visible with oxygen atoms run zig-zag horizontally in Fig. S1b. The corresponding structure factor calculations are shown in Figs. S1a',b', respectively. Note that while Fig. S1a' exhibits only fundamental reflections, such as $[001]_{pc}$, $[\bar{1}10]_{pc}$ and $[\bar{1}11]_{pc}$, extra reflections denoted by arrows show up together with the fundamental reflections in Fig. S1b'. This indicates that oxygen octahedral rotation in rhombohedral BFO causes extra reflections seen in diffraction patterns. Since the extra Bragg's reflections are clearly found in Fig. 1b, oxygen octahedral rotation is thought to be preserved in the current epitaxial BFO.

Note that rhombohedral symmetry found here is different than monoclinic symmetry found in an epitaxial BFO film grown on PSO substrate by Chen et al.[32] While they used X-ray reciprocal space mapping for out-of-plane and in-plane Bragg's peaks to accurately measure the slight shifts in Bragg's peak locations from those in bulk BFO, the symmetry of basis atom locations of the monoclinic phase was not provided in their study. Thus, it is hard to directly compare their study with the current study. Meanwhile, a more recent study on an epitaxial BFO film grown on PSO substrate using quantitative STEM technique concluded that the BFO film preserves rhombohedral-like feature, which agrees with the current study[47]. For convenience, let us call $[211]_h$ BFO domain "BFO I". The NBED pattern from PSO in Fig. 1c matches the $[\bar{1}11]_o$ zone axis of PSO with $(101)_o$ reflection along
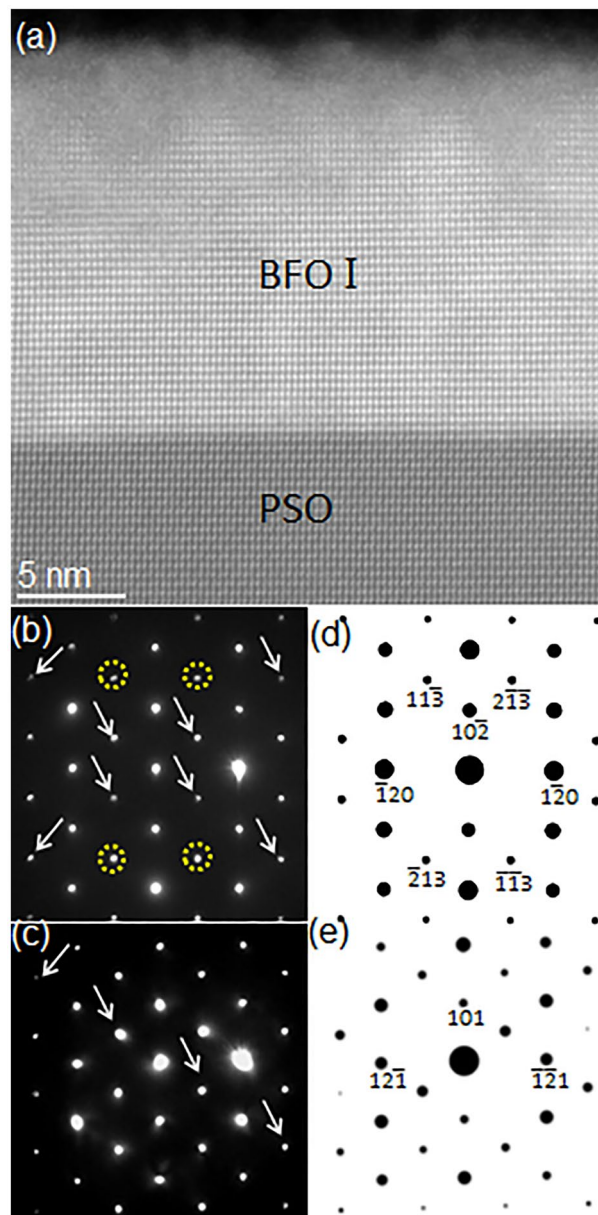
Figure 1. (**a**) A cross-sectional HAADF-STEM image of epitaxial BFO grown on PSO along $[\bar{1}11]_o$ zone axis with NBED patterns from (**b**) BFO I and (**c**) PSO together with their corresponding structure factor calculations in (**d**) and (**e**), respectively. (**d**) Confirms that (**b**) corresponds to $[211]_h$ rhombohedral BFO.

surface normal orientation (see Fig. 1e) as expected. The reflections resulting from dynamical scattering effect are denoted with white arrows in Fig. 1c[48]. Based on the results from Fig. 1d,e, the epitaxial relation between BFO I and PSO is as follows:

$[211]_h$ of BFO I // $[\bar{1}11]_o$ of PSO ; $(10\bar{2})_h$ of BFO I // $(101)_o$ of PSO.

Figure 2 shows an NBED pattern obtained from an area (using ~10 nm probe) that includes both BFO and PSO to identify whether the lattice misfit with PSO is stored as elastic strain in BFO layer or not. It can be readily noticed that the Bragg's reflections (denoted by white ellipses) from BFO and PSO split along out-of-plane orientations in Fig. 2a. Note that the split should occur radially if BFO is under no elastic strain as predicted by Fig. 2b that shows a structure factor calculation using *unstrained* BFO and *unstrained* PSO. In addition, the split of Bragg's reflections along out-of-plane orientation in Fig. 2a indicates the scattering vector components within BFO and PSO are the same along in-plane orientation. This means that the interplanar distances of BFO and PSO are the same along in-planed orientation. While the equilibrium, i.e., *unstrained*, interplanar distance of BFO along in-plane orientation, i.e., $BFO(1\bar{2}0)_h$, is 0.279 nm[45], the measured one is the same as interplanar distance of PSO along in-plane orientation, i.e., $PSO(\bar{1}2\bar{1})_o = 0.284$ nm[43]. Since the measured interplanar distance of $BFO(1\bar{2}0)_h$, i.e., 0.284 nm, is larger than unstrained one, i.e., 0.279 nm, BFO I is under tensile strain along in-plane orientation which is denoted with an arrow at the bottom-left in Fig. 2a.

Symmetry	Space group	Lattice parameter	Technique used	Year
Rhombohedral[44]	R3c	$a = 0.5678$ nm, $c = 1.3982$ nm, $a = b = 90°$, $g = 120°$	Neutron diffraction	2007
Monoclinic[45]	$P2_1/m$	$a = 0.5615$ nm, $b = 0.7973$ nm, $c = 0.5647$ nm, $a = 90°$, $b = 90°$, $g = 90.1°$	X-ray diffraction	2008
Tetragonal[21]	P4mm	$a = 0.367$ nm, $c = 0.464$ nm, $a = b = g = 90°$	First-principles	2006
Monoclinic[20]	Pc	$a = 0.7291$ nm, $b = 0.5291$ nm, $c = 0.5315$ nm, $a = 90°$, $b = 139.46°$, $g = 90°$	First-principles	2011
Monoclinic[20]	Cm	$a = 0.9354$ nm, $b = 0.7380$ nm, $c = 0.3804$ nm, $a = 90°$, $b = 86.60°$, $g = 90°$	First-principles	2011
Orthorhombic[20]	$Pna2_1$	$a = b = 0.5314$ nm, $c = 0.9452$ nm, $a = b = g = 90°$	First-principles	2011
Monoclinic[20]	Cc	$a = 1.0604$ nm, $b = 0.5322$ nm, $c = 0.5323$ nm, $a = 90°$, $b = 62.80°$, $g = 90°$	First-principles	2011
Orthorhombic[20]	Pnma	$a = 0.5650$ nm, b = 0.7770 nm, $c = 0.5421$ nm, $a = b = g = 90°$	First-principles	2011
Orthorhombic[20]	$Pna2_1$	$a = 0.5702$ nm, b = 0.5507 nm, $c = 0.8036$ nm, $a = b = g = 90°$	First-principles	2011
Orthorhombic-like monoclinic[27]	Cm	$a = 0.9262$ nm, $b = 0.7582$ nm, $c = 0.3791$ nm, $a = g = 90°$, $b = {\sim}90°$	Electron diffraction & First-principles	2017

Table 1. Summary of BFO phases that were previously reported with all the crystallographic information that includes lattice parameter, space group and basis location.
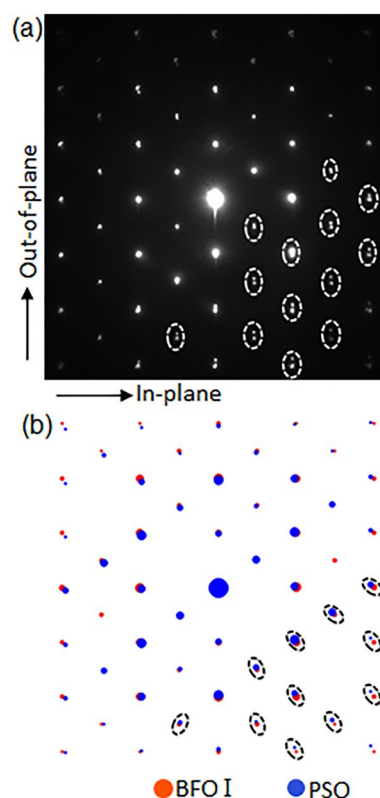

Figure 2. (**a**) A NBED pattern acquired from an area including BFO I and PSO substrate shown in Fig. 1(a, b) structure factor calculation result using unstrained BFO and unstrained PSO. The Bragg's reflections split vertically along out-of-plane orientation in (**a**), whereas those split radially in (**b**), indicating the in-plane components of BFO I scattering vectors are the same as that of PSO.

Figure 3a is a HAADF-STEM image of an adjacent area. While the contrast in BFO film appears similar with that in Fig. 1a, the NBED pattern from the area (see Fig. 3b) is distinctively different from Fig. 1b. Structure factor calculation revealed that Fig. 3b corresponds to $[0\bar{1}0]_h$ zone axis of rhombohedral BFO as shown in Fig. 3c[45]. Since this BFO domain has a different zone axis than BFO I shown in Fig. 1a, it is referred to as "BFO II". Based on the results from Figs. 1e and 3c, the epitaxial relation between BFO II and PSO is as follows:

$[0\bar{1}0]_h$ of BFO II // $[\bar{1}11]_o$ of PSO; $(10\bar{2})_h$ of BFO II // $(101)_o$ of PSO.

Figure 4a presents NBED patterns from both BFO II and PSO. The vertical split of BFO and PSO Bragg's reflections (denoted by white ellipses) is different from the radially oriented split (as denoted by black ellipses in Fig. 4b) that should occur between *unstrained* BFO and *unstrained* PSO. This indicates the scattering vectors of BFO II and PSO are the same along in-plane orientation, which is the same characteristic found between BFO I and PSO (see Fig. 2b). While the interplanar distance of *unstrained* BFO along in-plane orientation, i.e., BFO$(\bar{1}04)_h$ is 0.281 nm, the measured one is the same as interplanar distance of PSO along in-plane orientation, i.e., PSO$(\bar{1}2\bar{1})_o = 0.284$ nm[45], indicating that BFO II is under tensile strain for the same reason as for BFO I. It is worth noting that while the difference of *unstrained* in-plane lattices, i.e., $(1\bar{2}0)_h = 0.279$ nm for BFO I and $(\bar{1}04)_h = 0.281$ nm for BFO II can be distinguished based on the difference in NBED patterns shown in Figs. 1b and 3b, pc notations of the corresponding in-plane lattices for BFO I and BFO II are $(\bar{1}10)_{pc} = 0.280$ nm, and $(\bar{1}10)_{pc} = 0.280$ nm, respectively. This indicates pc notation cannot distinguish the difference.

The NBED data (showing that the interplanar distance of BFO is the same as that of PSO along the in-plane orientation) is further verified by X-ray reciprocal space mapping data as exhibited in Fig. S2. It provides a reciprocal space map from the vicinity of PSO$(2\bar{2}4)_o$ and BFO$(4\bar{2}6)_h$, i.e., BFO$(\bar{1}13)_{pc}$, peaks. Note that Q_z and Q_x are along PSO$[101]_o$, i.e., out-of-plane, and PSO$[\bar{1}2\bar{1}]_o$, i.e., in-plane, orientations, respectively. It is readily noticed that the in-plane components of scattering vectors, i.e., $Q_x/2\pi$, read 3.519 nm^{-1} for PSO$(2\bar{2}4)_o$ and 3.5191 nm^{-1} for BFO$(4\bar{2}6)_h$, i.e., BFO$(\bar{1}13)_{pc}$. This indicates the in-plane scattering components of BFO is the same as that of PSO, which is in good agreement with the NBED results shown in Figs. 2 and 4.

In order to provide a direct evidence of lattice misfit causing elastic strain within BFO, atomic resolution HAADF-STEM technique was employed as shown in Fig. 5. It can be readily noticed that PSO$(\bar{1}2\bar{1})_o$ lattice plane is commensurate with BFO lattice planes across BFO/PSO interface for both BFO I i.e., Fig. 5a, and BFO II, i.e., Fig. 5b. Besides, no misfit dislocations are found in BFO I and BFO II at the interfaces. Misfit dislocations often showing up as threading dislocations are known to play a role to relax elastic strain when dislocation density is higher than the threshold value (e.g., ~ 10^{11} cm^{-2} for $(Ba_xSr_{1-x})TiO_3$ film)[49,50]. Thus, it can be concluded that the epitaxial BFO in the present work is under *elastic* tensile strain caused by lattice misfit with PSO.
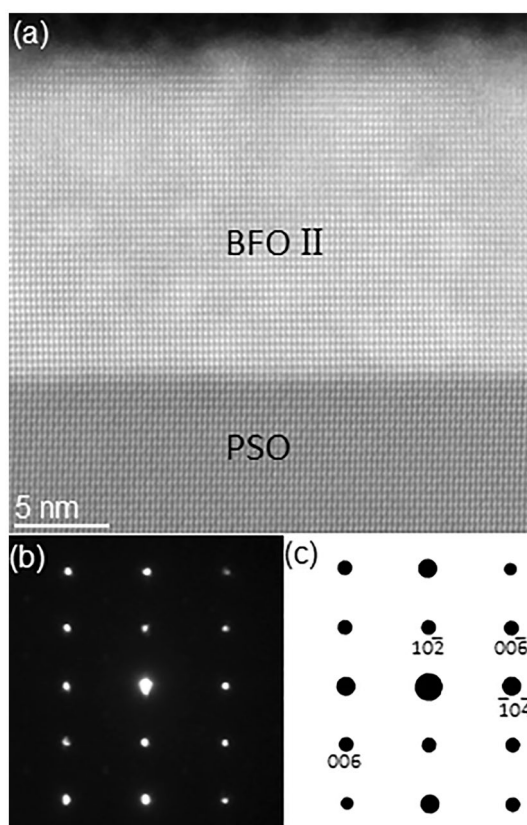

Figure 3. (**a**) A cross-sectional HAADF-STEM image from an area adjacent to Fig. 1a with (**b**) a NBED pattern from BFO II and (**c**) its corresponding structure factor calculation. (**c**) confirms that (**b**) corresponds to $[0\bar{1}0]_h$ rhombohedral BFO.

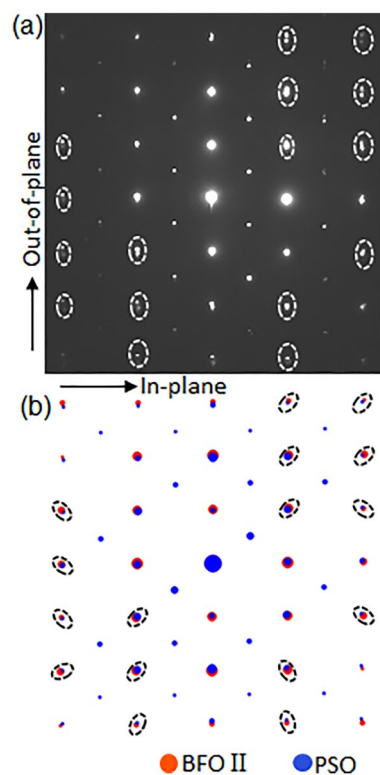**Figure 4.** (**a**) A NBED pattern acquired from an area including BFO II and PSO substrate shown in Fig. 3a, and (**b**) structure factor calculation result using unstrained BFO and unstrained PSO. The Bragg's reflections split vertically along out-of-plane orientation in (**a**) whereas those split radially in (**b**), indicating the in-plane components of BFO II scattering vectors are the same as that of PSO.
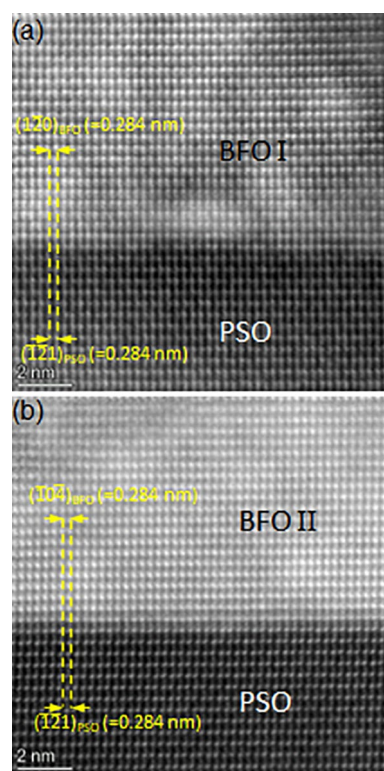

Figure 5. Lattice resolution HAADF-STEM images from (**a**) BFO I/PSO and (**b**) BFO II/PSO interfaces along PSO[$\bar{1}11$]$_o$ zone axis. The interplanar distances of BFO I and BFO II along in-plane orientation are the same as those of PSO with no signs of misfit dislocations at the interfaces.

6

The status of biaxial tensile strain across the entire BFO film is further investigated using precession electron diffraction technique (PED) with 120 keV electron and a precession angle of ~ 0.8°. In Fig. 6a is shown a virtual bright-field (BF) image was obtained using the direct beam, i.e., (000) central spot in diffraction pattern, from each PED pattern (see the insets at top right for BFO and bottom right for PSO as examples) as electron probe scans through the area. The interplanar distance along in-plane orientation at each pixel in Fig. 6a is calculated using high index Bragg's reflections as shown in the red cross hairs along red horizontal lines in the insets for high accuracy measurement. Figure 6b exhibits the ratio of interplanar distance difference along in-plane orientation, $\varepsilon_{xx} = \frac{d_{BFO(in-plane)} - d_{PSO(in-plane)}}{d_{PSO(in-plane)}}$. It is readily noticed that the contrast in BFO is even throughout the entire area except for the top right area with yellow, i.e., $\varepsilon_{xx} = \sim 0.006$, and green, i.e., $\varepsilon_{xx} = \sim 0.008$, shades. This may have to do with sample warpage or slight relaxation happening at the area. Note that some of the PED patterns from the area near top surface of BFO is excluded as they include the noise from neighboring amorphous Pt film that was deposited for FIB sample preparation (see the grayed-out area near the top surface of BFO enclosed with dotted lines in Fig. 6b). The mean and standard deviation of ε_{xx} from the entire area are -0.0009 and 0.0017, respectively. This confirms in-plane interplanar distance, i.e., $(1\bar{2}0)_h$, within BFO film is virtually the same as that in PSO, i.e., 0.284 nm, throughout the entire BFO area. This is in good agreement with NBED (see Figs. 2, 4) and lattice resolution HAADF-STEM (Fig. 5) results. Since the equilibrium interplanar distances of BFO I$(1\bar{2}0)_h$ and BFO II$(\bar{1}0\bar{4})_h$ along in-plane orientation are 0.279 nm and 0.281 nm[45], it becomes clear that
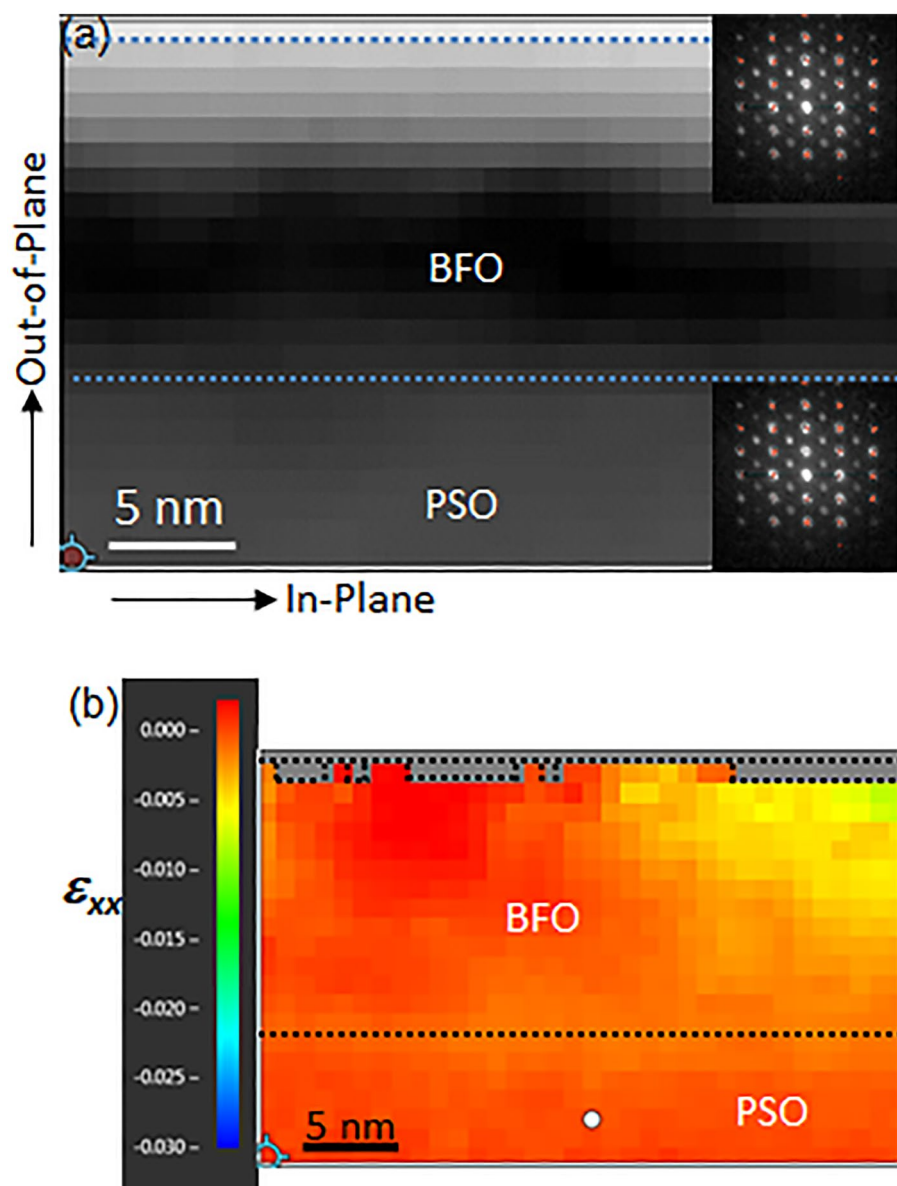

Figure 6. (a) A virtual BF image acquired from PED along PSO$[\bar{1}11]_o$ zone axis (with PED pattern examples from BFO and PSO shown as insets at top-right for BFO and at bottom-right for PSO), and (b) ε_{xx} extracted from PED patterns.

BFO layer is under tensile strain, i.e. ~ 1.79% for BFO I and ~ 1.06% for BFO II. Thus, the averaged tensile strain between BFO I and BFO II is ~ 1.43% along $[211]_h$, i.e., $[110]_{pc}$, orientation.

Another cross-sectional TEM sample is prepared along $PSO[010]_o$, a zone axis which is 45° away from $PSO[\bar{1}11]_o$ around the out-of-plane orientation to confirm the elastic strain status within BFO film as shown in Fig. 7. Figure 7a is a HAADF-STEM image showing ~ 20 nm thick BFO epitaxial layer grown on PSO. NBED patterns acquired from BFO and PSO are shown in Fig. 7b,c. It is worth noting that the NBED pattern in Fig. 7b can be interpreted either $[241]_h$ (see the indices in red) or $[2\bar{2}1]_h$ (see the indices in blue) of rhombohedral BFO as shown in Fig. 7d. Since $BFO[241]_h$ and $BFO[2\bar{2}1]_h$ are ~ 45° away from $BFO[211]_h$, i.e., BFO I, and $BFO[0\bar{1}0]_h$, i.e., BFO II, respectively, Fig. 7b corresponds to either BFO I or BFO II. Figure 7c matches the structure factor calculation of $PSO[\bar{1}11]_o$ as shown in Fig. 7e. The Bragg's reflections caused by dynamical scattering are denoted with white arrows in Fig. 7c[48]. An NBED pattern using ~ 10 nm probe that spanned the BFO/PSO interface is acquired to investigate elastic strain status within BFO layer as shown in Fig. 8. The Bragg's reflections aligned along out-of-plane orientation is readily found (see the white ellipses in Fig. 8a). This is the same characteristic, i.e., elastic tensile strain, as in Figs. 2 and 4, indicating that the interplanar distance of BFO is the same as that of PSO along in-plane orientation. This can be confirmed with an atomic resolution HAADF-STEM image in Fig. 9. It shows that PSO in-plane lattice, i.e., $PSO(\bar{1}01)_o$, is commensurate with BFO in-plane lattice, i.e., $(1\bar{1}2)_h$ of either BFO I or BFO II, with no signs of misfit dislocation. Note that while the measured interplanar distance of $(1\bar{1}2)_h$ of either BFO I or BFO II is 0.402 nm, i.e., the same as that of $PSO(\bar{1}01)_o$, in equilibrium it is 0.396 nm[43]. Thus, it is shown that BFO layer is under ~ 1.51% tensile strain along $PSO[010]_o$ orientation. The anisotropic elastic strain found here is in good agreement with the coherent tensile strain found along two in-plane orientations
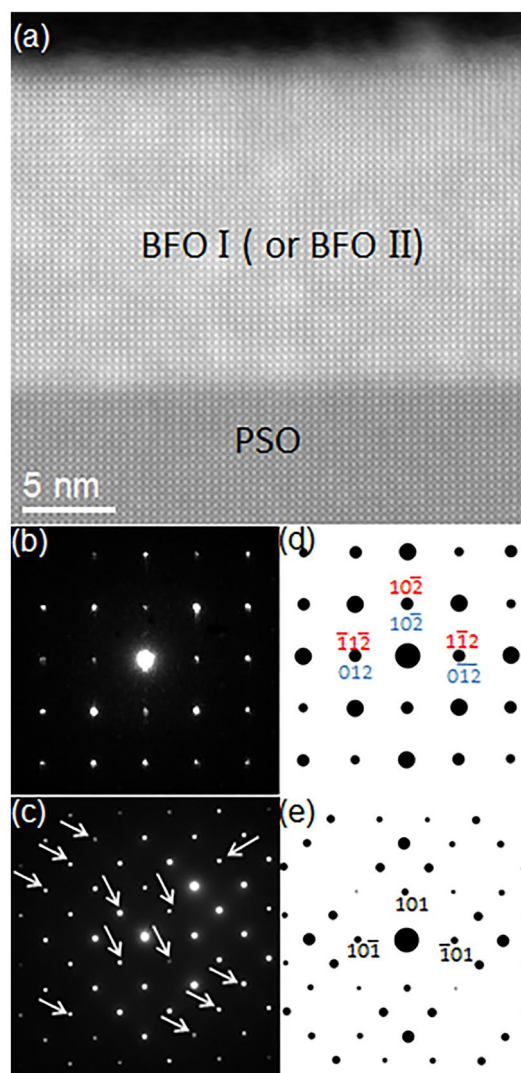

Figure 7. (a) A cross-sectional HAADF-STEM image of epitaxial BFO grown on PSO along $[010]_o$ zone axis with NBED patterns from (b) BFO and (c) PSO together with their corresponding structure factor calculations in (d) and (e), respectively. (d) Confirms that (b) corresponds to either $[241]_h$, i.e., BFO I, or $[2\bar{2}1]_h$, i.e., BFO II, of rhombohedral BFO.
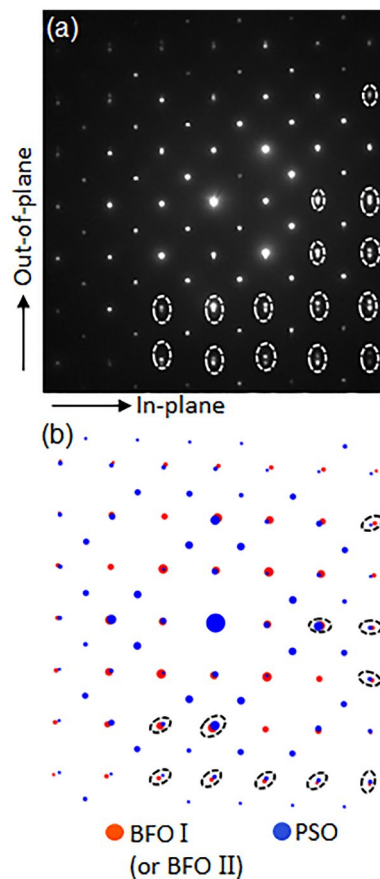
Figure 8. (**a**) A NBED pattern acquired from an area including BFO and PSO substrate shown in Fig. 7a, and (**b**) structure factor calculation result using unstrained BFO and unstrained PSO. The Bragg's reflections split vertically along out-of-plane orientation in (**a**) whereas those split radially in (**b**), indicating the in-plane components of BFO scattering vectors are the same as that of PSO.

within 13 nm-thick epitaxial BFO film grown on PSO substrate previously[32]. Based on the NBED analysis results in Figs. 2, 4 and 8, a schematic is drawn in Fig. 10 to visualize the epitaxial relations between BFO I and PSO (see Fig. 10a) and between BFO II and PSO (see Fig. 10b). It is also worth noting that BFO I and BFO II are 90° apart around the $(10\overline{2})_h$ plane normal, i.e., out-of-plane, orientation as discussed elsewhere[42].

Now let's turn our attention to interplanar distance within BFO along out-of-plane orientation. Note that both BFO I and BFO II have $(10\overline{2})_h$ plane along out-of-plane orientation as shown in Figs. 1 and 3. To precisely measure the volume averaged interplanar distance along out-of-plane orientation, X-ray diffraction technique is used with Cu Kα radiation, hybrid optics with Ge monochromator. In Fig. 11 is shown X-ray intensity as a function of 2θ acquired using θ–2θ geometry, i.e., out-of-plane orientation. A sharp peak located at 22.09° corresponds to PSO(101)$_o$ = 0.402 nm, whereas a broad peak at 22.89° is from BFO$(10\overline{2})_h$. Besides, thickness fringes are seen as well. The full width half maximum of BFO$(10\overline{2})_h$ is measured 0.254° which is much larger than 0.019° of PSO(101)$_o$ owing to peak broadening resulting from ~ 20 nm thickness of BFO film. The measured interplanar distance of BFO$(10\overline{2})_o$ based on 2θ = 22.89° turns out ~ 0.388 nm. Given the *unstrained* interplanar distance of BFO$(10\overline{2})_h$ is 0.396 nm, BFO film is under a uniaxial compressive strain (~ 2.02%) along out-of-plane orientation as the result of biaxial tensile strain along in-plane orientation. The uniaxial compressive strain of ~ 2.02% along out-of-plane orientation is larger than ~ 1.45% in-plane biaxial tensile strain averaged between PSO[010]$_o$,i.e., BFO[100]$_{pc}$, and PSO$[\overline{1}11]_o$ i.e., BFO[110]$_{pc}$ orientations. This is presumably due to the fact that while biaxial tensile strain is exerted two dimensionally across the entire BFO film, the tensile strain is uniaxial, i.e. one dimensional. Since two-dimensional tensile strain effect along in-plane orientation shows up one dimensional compressive strain along out-of-plane orientation, the out-of-plane compressive strain (~ 2.02%) turns out larger than in-plane tensile strain (~ 1.45%). This is in good agreement with the results on BFO film grown on KTaO₃ substrate previously[35].

By using the in-plane and out-of-plane strains, Poisson' ratio (ν), can be acquired as follows:

$ν = ε_{xx}/ε_{zz}/(ε_{zz}/ε_{xx} - 2)$, where $ε_{xx}$ and $ε_{zz}$ are in-plane and out-of-plane lattice mismatches, respectively[31,51]. ν for the current study turns out ~ 0.41. This is comparable to ν = ~ 0.49 reported previously using epitaxial BFO films grown on various oxide substrates[31]. This confirms the fact that BFO film possesses higher Poisson's ratio than other perovskite-based materials. The reason could be associated with structural flexibility within
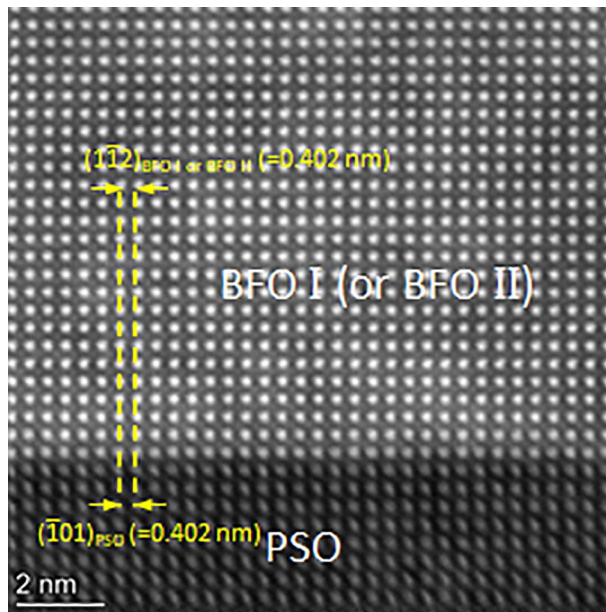
Figure 9. Atomic resolution HAADF-STEM images at BFO/PSO interface along PSO[010]o zone axis. The interplanar distances of BFO along in-plane orientation are the same as that of PSO with no signs of misfit dislocations at the interface. The BFO areas shown here could be either BFO I or BFO II as discussed for Fig. 7b,d.
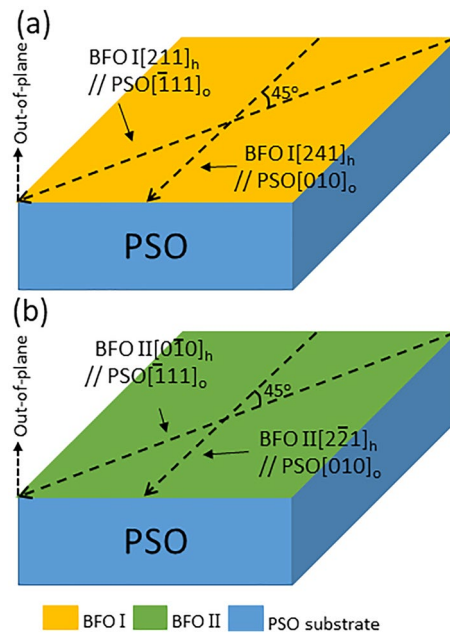

Figure 10. A schematic showing epitaxial relations: (**a**) between BFO I and PSO, and (**b**) BFO II and PSO. BFO I and BFO II are ~90° away around out-of-plane orientation.

perovskite-based BFO crystal structure that has already been discussed in terms of: (1) multiple metastable phases available[20,21] and (2) small perovskite tolerance factor (~0.88) allowing for large degrees of rotation and/or tilting of oxygen octahedra[31].

To further investigate ferroelectric domain structures and their relations with the crystallographically distinguished domain structures, i.e., BFO I and BFO II, 4D STEM DPC is performed along PSO[$\bar{1}$11]o zone axis as shown in Fig. 12. 4D STEM DPC technique collects a diffraction pattern at each pixel in a HAADF-STEM image (see Fig. 12a) and measures the displacement of the direct beam, i.e., central disk, in each diffraction
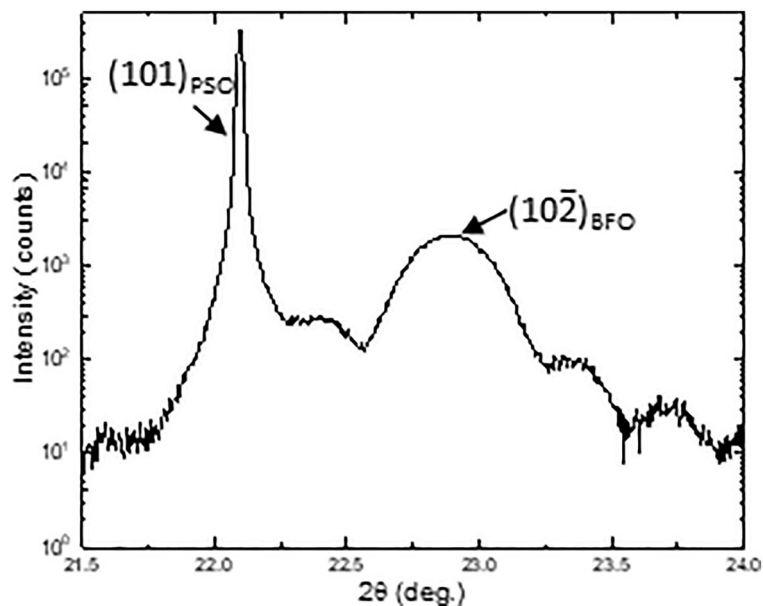
Figure 11. A XRD measurement with θ–2θ geometry, i.e., along out-of-plane orientation. A peak at 22.89° is from $\mathrm{BFO}(10\bar{2})_h$. Interplanar distance corresponding to 22.89° is ~ 0.388 nm which is smaller than that of *unstrained* $\mathrm{BFO}(10\bar{2})_h$, ~ 0.396 nm, indicating BFO film is under uniaxial compressive strain along out-of-plane orientation.
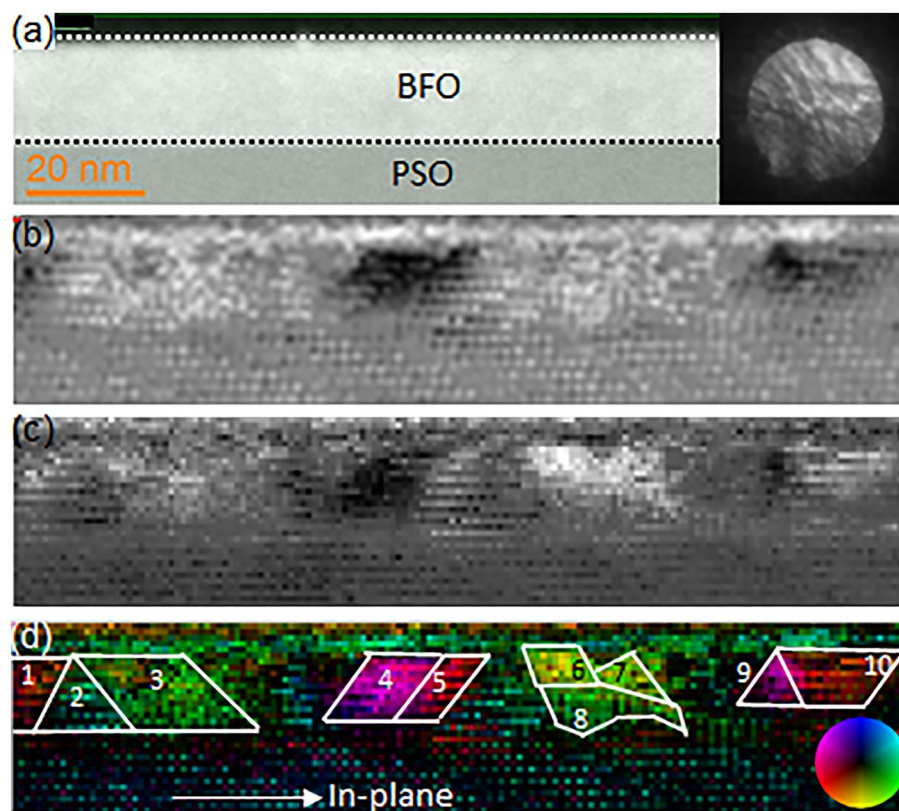

Figure 12. (**a**) A cross-sectional HAADF-STEM image of epitaxial BFO grown on PSO along $[\bar{1}11]_o$ zone axis with an example of direct beam, i.e., central disk in diffraction pattern, as an inset the right corner. Direct beam shifts, caused by the electric fields resulting from spontaneous polarization in dielectric domains are shown in terms of two orthogonal orientations, i.e., (**b**) *dx* and (**c**) *dy*. (**d**) Vector displacement map with a color wheel as an inset bottom right corner. Ferroelectric domains are denoted by white lines with numbers.

pattern. An example of direct beam recorded on a pixelated detector is shown an inset at the right corner in Fig. 12a. Note that the radius of the direct beam is 25 mrad. Then, the direct beam displacement, which occurs when incident electrons are deflected by the electric field due to spontaneous polarization within BFO ferroelectric domain[52], are calculated along two orthogonal orientations, i.e., *dx* (see Fig. 12b) and *dy* (see Fig. 12b) by center of mass approach[53]. The color-coded vector displacement map is calculated using *dx* and *dy* data as shown in Fig. 12d where the intensity scales to the magnitude of the vector field and the color represents its orientation as shown by the color wheel at bottom-right corner. While no clear contrast of ferroelectric domains is exhibited in a HAADF-STEM image obtained along PSO$[\bar{1}11]_o$ zone axis as shown in Fig. 12a, the vector displacement map in Fig. 12d clearly shows ferroelectric domains size of 10–20 nm. The polarization orientations of the ferroelectric domains (denoted 1–10) and their relations with crystallographic domains, i.e., BFO I and BFO II, are summarized in Table 2.

Note that (1) the angles are measured with respect to in-plane orientation denoted in Fig. 12d, and (2) the angles acquired from 10 pixels at the center of each domain were used to derive mean and standard deviation. It is worth noting that the domains with polarization angles 89.7° and 83.1° correspond to BFO I whereas the others correspond to BFO II. This has to do with the fact that while polarization orientation of BFO II has both of in-plane and out-of-plane components viewed along BFO$[110]_{pc}$//PSO$[\bar{1}11]_o$ zone axis [see the location of 006_h, i.e., 111_{pc}, reflection along which spontaneous polarization occurs in Fig. 3c], that of BFO I has out-of-plane components only. This is because the BFO I is 90° off BFO II around out-of-plane orientation as mentioned earlier (see Fig. 10)[42]. Han et al.[54] recently investigated spontaneous polarization orientations in epitaxial BFO grown on PSO$(001)_o$ substrate along $[110]_{pc}$ orientation using aberration corrected TEM to identify that, while 71° domain wall consists of polarization components of both in-plane and out-of-plane, 180° domain wall consists of out-of-plane component only. Thus, their result is consistent with the current study. In addition, the mean polarization angles of BFO II found here seem to be smaller with respect to in-plane orientation (except for domains 1 and 10), than the theoretical angle of 35.6°, as discussed elsewhere[42]. Although the standard deviations for the mean polarization angles in BFO I and BFO II are rather high, this might indicate the polarization orientations found here under biaxial tensile strain have more in-plane orientation component than that in unstrained BFO. It was reported that biaxial tensile strain could cause BFO polarization orientation to rotate within $(110)_{pc}$ plane towards in-plane orientation[32,55]. Note that $(110)_{pc}$ corresponds to the cross-section plane of BFO in Fig. 12 of which zone axis is $[211]_h$. Thus, the polarization orientations rotation towards in-plane orientation found for BFO I and BFO II seems to agree with those previous reports.

The polarization, i.e., ferroelectric, orientations summarized in Table 2 show four polarization, i.e., ferroelectric, variants (for example, see domains 1, 2, 3 and 4 whose angles with respect to the in-plane orientation denoted in Fig. 12d are 142.0°, −19.8°, 15.7°, and −155.6°, respectively). Thus, the result found here is different from two ferroelectric variants found in BFO grown on DyScO$_3$ (DSO) substrate, but consistent with the four ferroelectric variants found in BFO grown on STO buffered DSO substrate[56]. It is interesting to note that while 71° ferroelectric domain structure is dominantly found in the BFO grown on DSO substrate using PFM and X-ray reciprocal space mapping technique[56], the current study with BFO grown on PSO substrate found ferroelectric domain structures with angles other than the typical 71°, 109°, and 180° using 4D STEM DPC technique. For example, the angle between domains 1 and 4 is ~62°, whereas that between domains 2 and 3 is ~46° (see Table 2). This is the result of polarization orientation being rotated toward in-plane orientation owing to the tensile strain applied in the BFO as discussed earlier. It is unclear how the rotation of polarization orientation found in the current study would affect the ferroelectric domain structure and ferroelectric variants in BFO. Further study is needed to clarify this point.

| Domain | Angle with respect to in-plane orientation (deg.) | |
	Mean	SD
1 (BFO II)	142.0	8.4
2 (BFO II)	− 19.8	16.3
3 (BFO II)	25.7	8.6
4 (BFO II)	− 155.6	2.9
5 (BFO II)	161.6	8.0
6 (BFO I)	89.7	7.4
7 (BFO I)	83.1	11.2
8 (BFO II)	26.5	6.5
9 (BFO II)	− 158.6	4.8
10 (BFO II)	137.1	7.4

Table 2. Summary of the spontaneous polarization angles, i.e., mean and standard deviation, with respect to in-plane orientation for each ferroelectric domains denoted 1–10 in Fig. 12d. Note that the mean and standard deviation are based on 10 pixels from the central area of each ferroelectric domains denoted 1–10 in Fig. 12d. Their relations with crystallographic domains, i.e., BFO I and BFO II are also provided.

Summary

In summary, large biaxial tensile strain is investigated in an epitaxially grown BFO film on single crystalline PSO substrate in terms of BFO crystal symmetry, and ferroelectric domain structure using advanced STEM techniques. NBED patterns in comparison with structure factor calculations, along two zone axes showed no evidence of breakdown of rhombohedral symmetry, i.e., space group of *R3c*. However, lattice resolution STEM images, PED and XRD confirm that the misfit strain caused by PSO substrate is stored as elastic strain, i.e., ~ 1.45% biaxial tensile strain along in-plane orientation accompanied by ~ 2.2% uniaxial compressive strain along out-of-plane orientation, in the epitaxially grown BFO film. This results in a Poisson's ratio of ~ 0.41. In addition, two crystallogrphically distinguished BFO domains, i.e., BFO I and BFO II, are confirmed by NBED analysis. Their relations with ferroelectric domains are further studied using 4D STEM DPC technique. It visualizes: (1) ferroelectric domain sizes (10–20 nm) and (2) polarization orientation with the ferroelectric domains that have four ferroelectric variants. By combining polarization and the crystallographic orientation information, it is revealed that the ferroelectric domains showing only out-of-orientation component corresponds to BFO I, whereas those possessing both in-plane and out-of-plane components are BFO II. Larger in-plane polarization component found in BFO II than the theoretical one seems to agree with the tensile strain induced polarization rotation within BFO discussed in previous reports.

Methods

An epitaxial BFO film was grown on a $(101)_o$ PSO substrate using molecular beam epitaxy in PARADIM facility at Cornell University. Cross-sectional TEM samples were prepared using Thermo Fisher Helios 600 dual beam focused ion beam. Ga ion beam was gradually decreased from 30 to 2 kV to minimize ion beam induced damage. For HAADF-STEM, NBED and 4D STEM DPC, a Thermo Fisher Titan Themis G2 300 equipped with a probe corrector was used with a convergence semi-angle of 25 mrad, and 770 mm camera length. To minimize knock-on damage from incident electron to BFO film, 120 keV high tension was used to ensure that the maximum energy transfers to Bi, Fe, and O are below a typical threshold displacement energy of ~ 25 eV[57]. A Gatan OneView™ CMOS camera with readout binned to 512×512 pixels was used to collect diffraction data for 4D STEM DPC. Gatan Microscopy Suite software was used to analyze the 4D STEM DPC data. NBED patterns were calibrated using $(10\bar{2})$ and $(\bar{1}20)$ reflections from unstrained PSO substrate. For XRD analysis, Panalytical X'pert Pro with Cu Kα radiation was used in tandem with a hybrid optics equipped with Ge monochromator to measure out-of-plane Bragg's peak with high accuracy. X-ray reciprocal space mapping was performed using Rigaku SmartLab SE equipped with Cu Kα radiation, Ge(220) two bounce monochromator, and HyPix-400 2D detector.

Data availability

All data generated or analyzed during this study are included in the published article. In case, one wished to consult further information, it will be made available through the corresponding author on reasonable request.

References

1. Smolenskii, G. A. & Chupis, I. E. Segnetomagnetics. *Uspekhi Fiz. Nauk* **137**, 415–448. https://doi.org/10.3367/UFNr.0137.19820 7b.0415 (1982).
2. Kiselev, S. V., Ozerov, R. P. & Zhadanov, G. S. Detection of magnetic order in ferroelectric BiFeO₃ by neutron diffraction. *Sov. Phys. Dokl.* **7**, 742–744 (1963).
3. Eerenstein, W., Mathur, N. D. & Scott, J. F. Multiferroic and magnetoelectric materials. *Nature* **442**, 759–765. https://doi.org/10. 1038/nature05023 (2006).
4. Catalan, G. & Scott, J. F. Physics and applications of bismuth ferrite. *Adv. Mater.* **21**, 2463–2485. https://doi.org/10.1002/adma. 200802849 (2009).
5. Spaldin, N. A. & Ramesh, R. Advances in magnetoelectric multiferroics. *Nat. Mater.* **18**, 203–212. https://doi.org/10.1038/s41563- 018-0275-2 (2019).
6. Qi, X. D. *et al.* High-resolution X-ray diffraction and transmission electron microscopy of multiferroic BiFeO₃ films. *Appl. Phys. Lett.* **86**, 3. https://doi.org/10.1063/1.1866214 (2005).
7. Teague, J. R., Gerson, R. & James, W. J. Dielectric hysteresis in single crystal BiFeO₃. *Solid State Commun.* **8**, 1073–2000. https:// doi.org/10.1016/0038-1098(70)90262-0 (1970).
8. Wang, J. *et al.* Epitaxial BiFeO₃ multiferroic thin film heterostructures. *Science* **299**, 1719–1722. https://doi.org/10.1126/science. 1080615 (2003).
9. Lebeugle, D., Colson, D., Forget, A. & Viret, M. Very large spontaneous electric polarization in BiFeO₃ single crystals at room temperature and its evolution under cycling fields. *Appl. Phys. Lett.* **91**, 3. https://doi.org/10.1063/1.2753390 (2007).
10. Lebeugle, D. *et al.* Room-temperature coexistence of large electric polarization and magnetic order in BiFeO₃ single crystals. *Phys. Rev. B* **76**, 8. https://doi.org/10.1103/PhysRevB.76.024116 (2007).
11. Li, J. F. *et al.* Dramatically enhanced polarization in (001), (101), and (111) BiFeO₃ thin films due to epitiaxial-induced transitions. *Appl. Phys. Lett.* **84**, 5261–5263. https://doi.org/10.1063/1.1764944 (2004).
12. Tian, W. *et al.* Epitaxial integration of (0001) BiFeO₃ with (0001) GaN. *Appl. Phys. Lett.* **90**, 3. https://doi.org/10.1063/1.2730580 (2007).
13. Kim, D. H., Lee, H. N., Biegalski, M. D. & Christen, H. M. Effect of epitaxial strain on ferroelectric polarization in multiferroic BiFeO₃ films. *Appl. Phys. Lett.* **92**, 3. https://doi.org/10.1063/1.2830799 (2008).
14. Bea, H. *et al.* Crystallographic, magnetic, and ferroelectric structures of bulklike BiFeO₃ thin films. *Appl. Phys. Lett.* **93**, 3. https:// doi.org/10.1063/1.2940327 (2008).
15. Bea, H. *et al.* Evidence for room-temperature multiferroicity in a compound with a giant axial ratio. *Phys. Rev. Lett.* **102**, 5. https:// doi.org/10.1103/PhysRevLett.102.217603 (2009).
16. Zeches, R. J. *et al.* A strain-driven morphotropic phase boundary in BiFeO₃. *Science* **326**, 977–980. https://doi.org/10.1126/scien ce.1177046 (2009).

17. Singh, M. K., Ryu, S. & Jang, H. M. Polarized Raman scattering of multiferroic BiFeO$_3$ thin films with pseudo-tetragonal symmetry. *Phys. Rev. B* **72**, 4. https://doi.org/10.1103/PhysRevB.72.132101 (2005).
18. Naganuma, H., Oogane, M. & Ando, Y. Exchange biases of Co, Py, Co40Fe40B20, Co75Fe25, and Co50Fe50 on epitaxial BiFeO$_3$ films prepared by chemical solution deposition. *J. Appl. Phys.* **109**, 3. https://doi.org/10.1063/1.3563061 (2011).
19. Das, R. R. *et al.* Synthesis and ferroelectric properties of epitaxial BiFeO$_3$ thin films grown by sputtering. *Appl. Phys. Lett.* **88**, 3. https://doi.org/10.1063/1.2213347 (2006).
20. Dieguez, O., Gonzalez-Vazquez, O. E., Wojdel, J. C. & Iniguez, J. First-principles predictions of low-energy phases of multiferroic BiFeO$_3$. *Phys. Rev. B* **83**, 13. https://doi.org/10.1103/PhysRevB.83.094105 (2011).
21. Ricinschi, D., Yun, K. Y. & Okuyama, M. A mechanism for the 150 mu C cm(−2) polarization of BiFeO$_3$ films based on first-principles calculations and new structural data. *J. Phys.-Condes. Matter* **18**, L97–L105. https://doi.org/10.1088/0953-8984/18/6/l03 (2006).
22. Chen, Z. H. *et al.* Nanoscale domains in strained epitaxial BiFeO$_3$ thin Films on LaSrAlO$_4$ substrate. *Appl. Phys. Lett.* **96**, 3. https://doi.org/10.1063/1.3456729 (2010).
23. Christen, H. M., Nam, J. H., Kim, H. S., Hatt, A. J. & Spaldin, N. A. Stress-induced R-M-A-M-C-T symmetry changes in BiFeO$_3$ films. *Phys. Rev. B* **83**, 7. https://doi.org/10.1103/PhysRevB.83.144107 (2011).
24. Liu, H., Yang, P., Yao, K. & Wang, J. Growth rate induced monoclinic to tetragonal phase transition in epitaxial BiFeO$_3$ (001) thin films. *Appl. Phys. Lett.* **98**, 102902. https://doi.org/10.1063/1.3561757 (2011).
25. Pailloux, F. *et al.* Atomic structure and microstructures of supertetragonal multiferroic BiFeO$_3$ thin films. *Phys. Rev. B* **89**, 9. https://doi.org/10.1103/PhysRevB.89.104106 (2014).
26. Yang, J. C. *et al.* Orthorhombic BiFeO$_3$. *Phys. Rev. Lett.* **109**, 247606. https://doi.org/10.1103/PhysRevLett.109.247606 (2012).
27. Bae, I. T. *et al.* Elucidation of crystal and electronic structures within highly strained BiFeO$_3$ by transmission electron microscopy and first-principles simulation. *Sci. Rep.* **7**, 12. https://doi.org/10.1038/srep46498 (2017).
28. Saito, K. *et al.* Structural characterization of BiFeO$_3$ thin films by reciprocal space mapping. *Jpn. J. Appl. Phys.* **45**, 7311. https://doi.org/10.1143/JJAP.45.7311 (2006).
29. Xu, G. Y., Li, J. F. & Viehland, D. Ground state monoclinic (M-b) phase in (110)(c) BiFeO$_3$ epitaxial thin films. *Appl. Phys. Lett.* **89**, 3. https://doi.org/10.1063/1.2392818 (2006).
30. Liu, H. *et al.* Thickness-dependent twinning evolution and ferroelectric behavior of epitaxial BiFeO$_3$ (001) thin films. *Phys. Rev. B* **82**, 064108. https://doi.org/10.1103/PhysRevB.82.064108 (2010).
31. Chen, Z. H. *et al.* Low-symmetry monoclinic phases and polarization rotation path mediated by epitaxial strain in multiferroic BiFeO$_3$ thin films. *Adv. Funct. Mater.* **21**, 133–138. https://doi.org/10.1002/adfm.201001867 (2011).
32. Chen, Z. H. *et al.* Large tensile-strain-induced monoclinic M-B phase in BiFeO$_3$ epitaxial thin films on a PrScO$_3$ substrate. *Phys. Rev. B* **88**, 6. https://doi.org/10.1103/PhysRevB.88.054114 (2013).
33. Sando, D., Xu, B., Bellaiche, L. & Nagarajan, V. A multiferroic on the brink: Uncovering the nuances of strain-induced transitions in BiFeO$_3$. *Appl. Phys. Rev.* **3**, 16. https://doi.org/10.1063/1.4944558 (2016).
34. Paull, O. *et al.* Anisotropic epitaxial stabilization of a low-symmetry ferroelectric with enhanced electromechanical response. *Nat. Mater.* **21**, 74–80. https://doi.org/10.1038/s41563-021-01098-w (2022).
35. Bae, I. T. *et al.* Tensile stress effect on epitaxial BiFeO$_3$ thin film grown on KTaO$_3$. *Sci. Rep.* **8**, 9. https://doi.org/10.1038/s41598-018-19487-8 (2018).
36. Schlom, D. G. *et al.* Elastic strain engineering of ferroic oxides. *MRS Bull.* **39**, 118–130. https://doi.org/10.1557/mrs.2014.1 (2014).
37. Sando, D., Barthelemy, A. & Bibes, M. BiFeO$_3$ epitaxial thin films and devices: Past, present and future. *J. Phys.-Condes. Matter* **26**, 23. https://doi.org/10.1088/0953-8984/26/47/473201 (2014).
38. Bae, I. T. & Naganuma, H. Evidence of rhombohedral structure within BiFeO$_3$ thin film grown on SrTiO$_3$. *Appl. Phys. Express* **8**, 4. https://doi.org/10.7567/apex.8.031501 (2015).
39. Bae, I. T., Naganuma, H., Ichinose, T. & Sato, K. Thickness dependence of crystal and electronic structures within heteroepitaxially grown BiFeO$_3$ thin films. *Phys. Rev. B* **93**, 6. https://doi.org/10.1103/PhysRevB.93.064115 (2016).
40. Bae, I. T. *et al.* Strategy to utilize transmission electron microscopy and X-ray diffraction to investigate biaxial strain effect in epitaxial BiFeO$_3$ films. *Jpn. J. Appl. Phys.* **57**, 12. https://doi.org/10.7567/jjap.57.0902a5 (2018).
41. Bae, I. T. *et al.* Short range biaxial strain relief mechanism within epitaxially grown BiFeO$_3$. *Sci. Rep.* **9**, 10. https://doi.org/10.1038/s41598-019-42998-x (2019).
42. Bae, I. T. *et al.* Growth mechanism and domain structure study on epitaxial BiFeO$_3$ film grown on (La$_{0.3}$Sr$_{0.7}$)(Al$_{0.65}$Ta$_{0.35}$)O$_3$. *J. Appl. Phys.* **127**, 8. https://doi.org/10.1063/5.0005672 (2020).
43. Gesing, T. M., Uecker, R. & Buhl, J.-C. Refinement of the crystal structure of praseodymium orthoscandate, PrScO$_3$. *Z. Krist. New Cryst. Struct.* **224**, 365–366. https://doi.org/10.1524/ncrs.2009.0159 (2009).
44. Williams, D. B. & Carter, C. B. *Transmission Electron Microscopy* 379 (Springer, 2009).
45. Palewicz, A., Przenioslo, R., Sosnowska, I. & Hewat, A. W. Atomic displacements in BiFeO$_3$ as a function of temperature: neutron diffraction study. *Acta Crystallogr. Sect. B-Struct. Sci. Cryst. Eng. Mater.* **63**, 537–544. https://doi.org/10.1107/s0108768107023956 (2007).
46. Haumont, R. *et al.* Phase stability and structural temperature dependence in powdered multiferroic BiFeO$_3$. *Phys. Rev. B* **78**, 8. https://doi.org/10.1103/PhysRevB.78.134108 (2008).
47. Wang, W.-Y. *et al.* Atomic mapping of structural distortions in 109° domain patterned BiFeO$_3$ thin films. *J. Mater. Res.* **32**, 2423–2430. https://doi.org/10.1557/jmr.2017.206 (2017).
48. Williams, D. B. & Carter, C. B. *Transmission Electron Microscopy* 2nd edn, 265 (Springer, 2009).
49. Canedy, C. L. *et al.* Dielectric properties in heteroepitaxial Ba$_{0.6}$Sr$_{0.4}$TiO$_3$ thin films: Effect of internal stresses and dislocation-type defects. *Appl. Phys. Lett.* **77**, 1695–1697. https://doi.org/10.1063/1.1308531 (2000).
50. Misirlioglu, I. B., Vasiliev, A. L., Aindow, M., Alpay, S. P. & Ramesh, R. Threading dislocation generation in epitaxial (Ba, Sr) TiO$_3$ films grown on (001) LaAlO$_3$ by pulsed laser deposition. *Appl. Phys. Lett.* **84**, 1742–1744. https://doi.org/10.1063/1.1664035 (2004).
51. Kossoy, A., Wachtel, E. & Lubomirsky, I. On the Poisson ratio and XRD determination of strain in thin films of Ce$_{0.8}$Gd$_{0.2}$O$_{1.9}$. *J. Electroceram.* **32**, 47–50. https://doi.org/10.1007/s10832-013-9835-7 (2014).
52. Lohr, M. *et al.* Differential phase contrast 2.0-Opening new "fields" for an established technique. *Ultramicroscopy* **117**, 7–14. https://doi.org/10.1016/j.ultramic.2012.03.020 (2012).
53. Müller, K. *et al.* Atomic electric fields revealed by a quantum mechanical approach to electron picodiffraction. *Nat. Commun.* **5**, 5653. https://doi.org/10.1038/ncomms6653 (2014).
54. Han, M. J. *et al.* Mapping gradient-driven morphological phase transition at the conductive domain walls of strained multiferroic films. *Phys. Rev. B* **100**, 104109. https://doi.org/10.1103/PhysRevB.100.104109 (2019).
55. Jang, H. W. *et al.* Strain-induced polarization rotation in epitaxial (001) BiFeO$_3$ thin films. *Phys. Rev. Lett.* **101**, 107602. https://doi.org/10.1103/PhysRevLett.101.107602 (2008).
56. Chen, Z. H., Damodaran, A. R., Xu, R., Lee, S. & Martin, L. W. Effect of "symmetry mismatch" on the domain structure of rhombohedral BiFeO$_3$ thin films. *Appl. Phys. Lett.* https://doi.org/10.1063/1.4875801 (2014).
57. Williams, D. B. & Carter, C. B. *Transmission Electron Microscopy* 2nd edn, 67 (Springer, 2009).

Acknowledgements

Author contributions

I.T.B., and H.P. conceived the study. H.P. deposited the film. I.T.B., Z.R.L., and B.J.F. performed FIB and TEM. P.M.A. performed XRD. I.T.B. wrote the manuscript with inputs from all authors. All authors have given approval to the final version of the manuscript.

Competing interests

The authors declare no competing interests.

Additional information

Supplementary Information The online version contains supplementary material available at https://doi.org/10.1038/s41598-023-45980-w.

Correspondence and requests for materials should be addressed to I.-T.B.

Reprints and permissions information is available at www.nature.com/reprints.

Publisher's note Springer Nature remains neutral with regard to jurisdictional claims in published maps and institutional affiliations.